

Simultaneous Imaging of Artery-Wall Strain and Blood Flow by High Frame Rate Acquisition of RF Signals

Hideyuki Hasegawa, *Member, IEEE*, and Hiroshi Kanai

Abstract—Mechanical properties of the arterial walls are significantly altered by atherosclerosis, and various studies have been recently conducted to measure the regional elastic properties (radial strain) of the arterial wall. We have developed a phase-sensitive correlation-based method, namely, the phased-tracking method, to measure the regional radial strain. On the other hand, the measurement of blood flow is an important practical routine in the diagnosis of atherosclerosis. It would be useful if the regional strain of the arterial wall as well as blood flow could be assessed simultaneously. Such measurement would require a high frame rate of several kilohertz. In this study, acquisition of ultrasonic RF echoes at a high frame rate (about 3500 Hz) was achieved using parallel beamforming in which plane waves were transmitted only 3 times and receive beamforming created 24 beams for each transmit beam. The accuracy in measurement of the minute radial strain was evaluated by a basic experiment using a cylindrical phantom. The error of the measured strain from the theoretical strain profile and its standard deviation were 4.8% and 9.5%, respectively. Furthermore, the radial strain of a carotid arterial wall and blood flow were simultaneously imaged *in vivo*.

I. INTRODUCTION

PATHOLOGICAL change of the arterial wall due to atherosclerosis leads to a significant change in its mechanical properties [1], [2]. Most conventional methods for noninvasive measurement of elasticity are based on measurement of the pulse wave velocity [3]–[6] or that of the change in diameter [7]–[10]. Although these methods are useful in terms of their ability to assess the vascular elasticity noninvasively, the elasticity evaluated by these methods corresponds to the average elasticity in the direction of propagation and the entire circumference.

Elastography was introduced by Ophir *et al.* to measure the strain distribution of biological tissue by cross-correlating 2 different RF signals, namely, that before and that after deformation [11]–[14]. Then de Korte *et al.* applied elastography for strain imaging of the arterial wall with intravascular ultrasonography (IVUS), namely, intravascular elastography [15], [16]. In the cited studies, the elasticity distribution of coronary atherosclerotic plaque was obtained by the measured displacement distribution in the radial direction. This measured elasticity distribution was compared with the pathological image, the re-

sults suggesting the potential for tissue characterization of atherosclerotic plaque by measurement of its elasticity.

As a transcatheter approach, the displacement and strain around carotid atherosclerotic plaque have been measured using tissue Doppler imaging [17]. The inhomogeneity of displacements measured upstream and downstream of atherosclerotic plaque suggests that artery-wall motion has potential for use in the evaluation of plaque vulnerability. Furthermore, studies on noninvasive vascular elastography have also been conducted [18]–[20]. In most of the above-mentioned methods, a correlation-based technique is used for the estimation of the displacement and strain of the arterial wall [15]–[18], [21]. Also, in recent years, iterative methods have been introduced for estimating 2-D displacement [19], [22].

We have been studying the measurement of the displacement and radial strain (change in thickness) of the arterial wall based on the phase-sensitive correlation-based technique and have developed the phased-tracking method [23]–[27]. Elasticity images of the human carotid artery have been obtained based on the measured strain distribution, and the potential for transcatheter tissue characterization has been shown by classifying the elasticity images using the elasticity reference data obtained by *in vitro* experiments [28]–[31].

On the other hand, the measurement of blood flow is an important practical routine in clinical situations, and the interaction between blood flow and characteristics of the arterial wall is also important in the diagnosis of atherosclerosis. Plett *et al.* measured high-frequency vibrations on the arterial wall around atherosclerotic plaque based on the Doppler technique using a fixed ultrasonic beam [32]. They hypothesized that such vibrations were caused by turbulence of blood flow around plaque. Such irregular vibrations and motion of the arterial wall may promote the vulnerability of atherosclerotic plaque.

The shear stress acting on the luminal surface of the arterial wall is an important factor of the atherosclerotic change of the arterial wall. Tortoli *et al.* developed a system that simultaneously measured the distension of the carotid arterial wall and blood flow using 2 ultrasonic beams [33]. They measured the true blood flow velocity using 2 ultrasonic beams to estimate the wall shear rate, together with the distension of the arterial wall.

It has been reported that the artery dilates when blood flow increases because endothelial cells produce nitric oxide, which relaxes smooth muscle in the media, in response to the shear stress due to blood flow. Therefore,

Manuscript received March 2, 2008; accepted July 8, 2008.

H. Hasegawa and H. Kanai are with Department of Electronic Engineering, Graduate School of Engineering, Tohoku University, Sendai, Japan (email: hasegawa@us.ecei.tohoku.ac.jp).

Digital Object Identifier 10.1109/TUFFC.2008.978

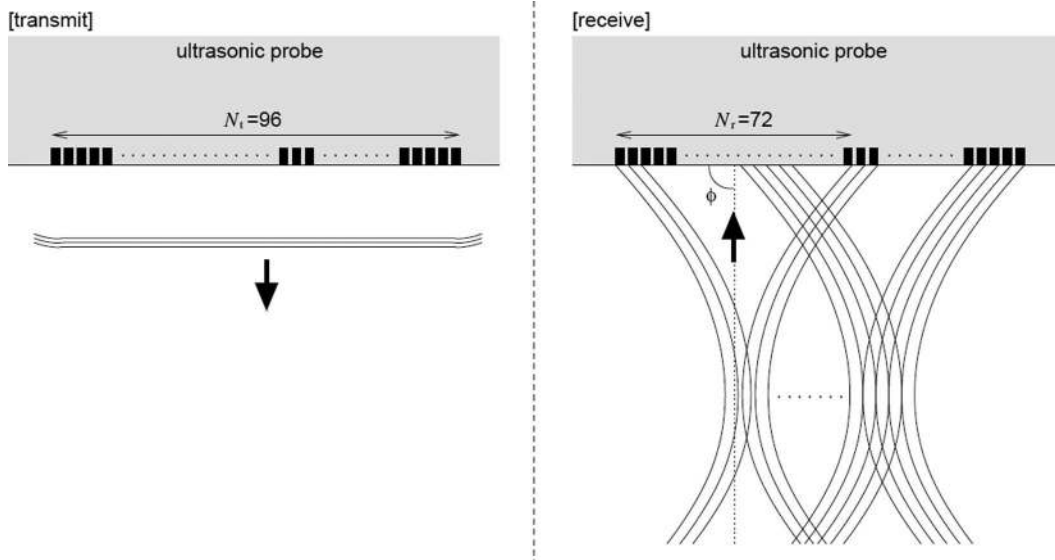


Fig. 1. Illustration of one transmit-receive procedure in parallel beamforming.

the endothelial function can be evaluated by measuring the dilation of the artery or the change in the mechanical property of the wall [34]–[36].

In these studies, blood flow and characteristics of the arterial wall (e.g., vibration and elasticity) were not imaged simultaneously. Therefore, it would be useful if the regional strain of the arterial wall and blood flow could be assessed simultaneously. Such measurement would require a high frame rate of several kilohertz. In this study, a high frame rate acquisition of ultrasonic RF echoes (about 3500 Hz) was achieved using parallel beam forming [37]–[42]. The accuracy in measurement of the minute radial strain was evaluated by a basic experiment using a cylindrical phantom. Furthermore, the radial strain of a carotid arterial wall and blood flow were simultaneously imaged *in vivo*.

II. PRINCIPLES

A. Parallel Beamforming

In conventional linear scanning, both transmit and receive beamforming are performed. Therefore, the frame rate, f_{FR} , is determined by dividing the pulse repetition frequency (PRF), f_{PRF} , by the number of beams, N_{bm} . Typically, frame rate f_{FR} is about 140 Hz when $f_{PRF} = 10\,000$ Hz and $N_{bm} = 72$.

On the other hand, only receive beamforming is performed in parallel beamforming. Many beams are created by receive beamforming for each transmission of a wide beam. For example, a frame rate f_{FR} of about 3300 Hz can be achieved when $f_{PRF} = 10\,000$ Hz and the number of transmissions, N_{tr} , is 3. Parallel beamforming achieves a high frame rate at the expense of the spatial resolution because transmit beamforming is not performed.

In this study, a plane wave was transmitted using $N_t = 96$ elements of a linear array probe equipped to a commercial diagnostic system (α -10, Aloka, Tokyo, Japan), and RF echoes were received by the same 96 elements. Fig. 1 shows an illustration of one transmit-receive procedure. One receiving beam was formed using the RF signals received by $N_c = 72$ of the 96 elements. Therefore, $(N_t - N_c) = 24$ receiving beams could be formed for each transmission.

The number of transmissions, N_{tr} , was set at 3, and the element number, $\{n_i\}$, used for i -th transmission ($i = 0, 1, \dots, N_{tr}$) is expressed as follows:

$$n_i = (N_t - N_c) \cdot i + j. \quad (j = 0, 1, 2, \dots, N_c) \quad (1)$$

By performing receive beamforming for each of the 3 transmissions, $(N_t - N_c) \cdot N_{tr} = 72$ receiving beams were created. In the receive beamforming, focusing was performed with respect to each sampled point in the scanned region. Pulse repetition frequency f_{PRF} was set at 10 416 Hz (observable depth: 74 mm), and a frame rate f_{FR} of 3472 Hz was achieved. In the present study, the RF signal received by each of the 96 elements was acquired at a sampling frequency of 40 MHz for offline processing (receive beamforming, calculations of strain and blood flow).

In this study, the imaging plane and the surface of the linear array probe were parallel to the arterial longitudinal direction. Under such condition, the receiving beam at an angle, ϕ (in Fig. 1), of 90 degrees coincided with the arterial radial direction. Therefore, receiving beams at $\phi = 90$ degrees were formed to estimate the radial strain of the arterial wall. For imaging of blood flow, receiving beams at $\phi = 70$ and 110 degrees were formed. As shown in Fig. 2, these beamformed RF signals were combined for simultaneous imaging of the radial strain and blood flow. Images of the radial strain of the arterial wall and blood

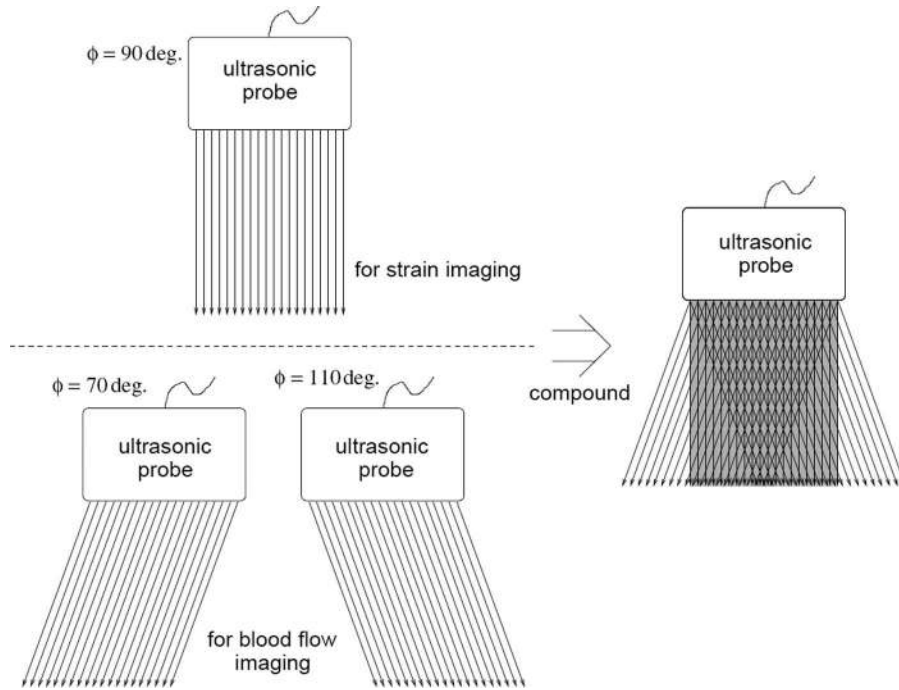


Fig. 2. Illustration of simultaneous imaging of artery wall strain and blood flow.

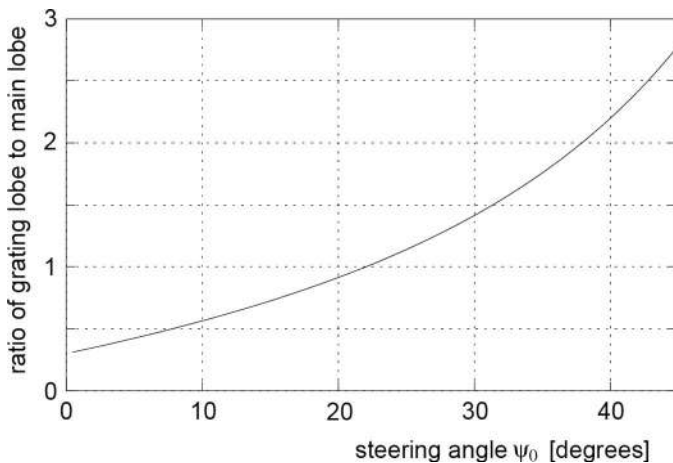


Fig. 3. Ratio $\gamma(\psi_0)$ of the magnitude of the grating lobe to that of the main lobe plotted as a function of steering angle ψ_0 .

flow in the shadowed region in the right-hand side of Fig. 2 were obtained.

The angles of the receiving beams for blood flow measurement were determined by theoretical consideration of the magnitude of the grating lobe (see the appendix) [43]. By considering the parameters employed in this study, wavelength $\lambda = 150 \mu\text{m}$ (at speed of sound $c_0 = 1500 \text{ m/s}$ and center frequency $f_0 = 10 \text{ MHz}$), element pitch $d = 200 \mu\text{m}$, and $w/\lambda \approx 1$, it is found that the magnitude of the grating lobe becomes larger than that of the main lobe when the steering angle ψ_0 is larger than 22 degrees. Fig. 3 shows the ratio, $\gamma(\psi_0)$, of the magnitude of the grating lobe to that of the main lobe theoretically calculated by (10) in the appendix. Therefore, in this study, the steering

angle ψ_0 was set to 20 degrees, which corresponds to the beam angles ϕ of 70 and 110 degrees. The ratio $\gamma(\psi_0)$ at $\psi_0 = 20$ degrees ($\phi = 70$ and 110 degrees) is 0.913.

The beamformed RF signals at $\phi = 90$ degrees were processed as described in the following sections to estimate the radial strain. For imaging of blood flow, a standard double delay line canceler [44] was used for high-pass filtering of the beamformed RF signals at $\phi = 70$ and 110 degrees. The power of the high-pass filtered RF signals was estimated and displayed based on the conventional power Doppler technique.

B. Tracking of Global Motion of the Arterial Wall

As shown in Fig. 4, the position of the peak in the correlation function $c_{k_m}(i; \tau)$ between RF signals $s(x; k_m)$ and $s(x = c_0\tau/2; k_m + i)$ in the k_m th and $(k_m + i)$ th frames at depths x and $x + c_0\tau/2$ moves in relation to the movement of the arterial wall in the direction of an ultrasonic beam, where k_m is defined as the frame number of the m th key frame ($k_0 = 0$). The region of interest (ROI) in ultrasound data, which corresponds to the region for calculation of correlation function $c_{k_m}(i; \tau)$, was determined by manually assigning the depths of the lumen-intima and media-adventitia boundaries, $x_1(k_m)$ and $x_N(k_m)$, of the arterial wall in the first frame ($k_m = k_0 = 0$) because an automated segmentation method was not developed in the present study. The ROI position in another frame ($k_m \neq 0$) is automatically determined by the procedure described below. The global displacement of the arterial wall must be determined from the sampled version of the correlation function (shown by the filled circles in Fig. 4) because RF

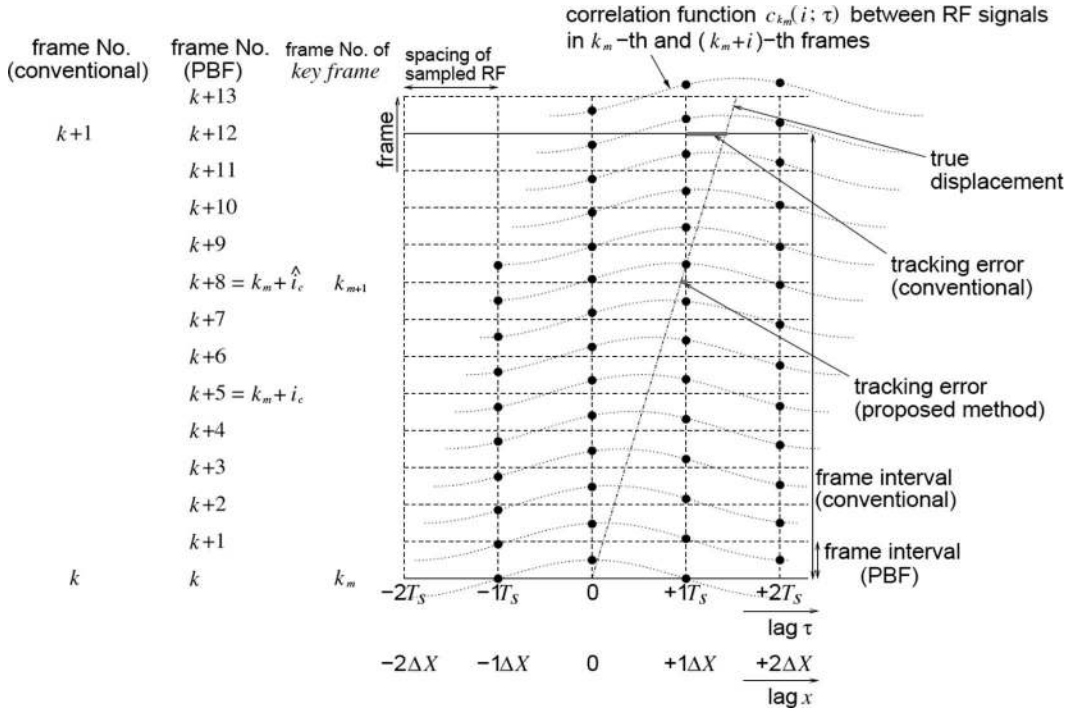


Fig. 4. Illustration of correlation-based tracking (PBF: parallel beamforming).

signals $\{s(x; k)\}$ (k : frame number) are sampled at a sampling frequency of $f_s = 1/T_s$. In Fig. 4, $\Delta X = c_0 T_s/2$. is the sampling interval in length.

In conventional ultrasonic equipment based on linear scanning, as shown in Fig. 4, neither the frame rate f_{FR} nor the sampling frequency f_s are high. In this case, the displacement is estimated by finding the discrete lag $\hat{\tau}$ ($= +T_s$ in Fig. 4), which gives the maximum value of sampled correlation function $c_k(i; \tau)$ between RF signals $s(x; k)$ and $s(x + c_0\tau/2; k + 1)$, in the direction of lag τ . Theoretically, the maximum tracking error is half the sampling interval ($\Delta X/2 = (1540 \text{ m/s})/(40 \text{ MHz})/2/2 = 9.6 \mu\text{m}$). On the other hand, in parallel beamforming, frame rate $f_{FR} = 3472 \text{ Hz}$ is much higher than that in conventional linear scanning, whereas sampling frequency f_s is the same. Therefore, as shown in Fig. 4, the change in the position of the peak in the correlation function between 2 consecutive frames is much smaller than sampling interval T_s . In this study, 2 frames ($= k_m$ and $k_m + \hat{i}_c = k_{m+1}$ in Fig. 4), between which the global displacement of the arterial wall is closest to one sampling interval T_s , can be determined by finding the frame $k_m + \hat{i}_c$ ($\hat{i}_c = 8$ in Fig. 4), which gives the maximum value of sampled correlation function $c_{k_m}(i; \tau)$, in the direction of frame i at a certain lag τ ($= +T_s$ in Fig. 4). In other words, the displacement between k_m th and $(k_m + \hat{i}_c)$ th frames is determined to be $c_0 T_s/2$. The maximum tracking error in this case depends on the displacement of the arterial wall between 2 consecutive frames. It becomes $(10 \text{ mm/s})/(3472 \text{ Hz}) = 2.9 \mu\text{m}$ when

the velocity of the arterial wall and frame rate are 10 mm/s and 3472 Hz, respectively.

The lag τ ($= +T_s$ in Fig. 4) at which the maximum value of sampled correlation function $c_{k_m}(i; \tau)$ is searched for in the direction of frame is determined as follows: As described above, the displacement of the arterial wall between 2 consecutive frames is much smaller than the spacing of sampled points in parallel beamforming. Therefore, it is sufficient to evaluate correlation functions $\{c_{k_m}(i; \tau)\}$ at lags $\tau = 0, \pm T_s$, and $\pm 2T_s$ for each i ($= 0, 1, 2, \dots$). When $c_{k_m}(i; T_s)$ [or $c_{k_m}(i; -T_s)$] becomes larger than $c_{k_m}(i; 0)$ in the $(k_m + i_c)$ th frame, the frame, \hat{i}_c ($> i_c$), in which $c_{k_m}(\hat{i}_c; T_s)$ [or $c_{k_m}(\hat{i}_c; -T_s)$] is maximum, is searched for in the direction of the frame until $c_{k_m}(\hat{i}_c; T_s)$ [or $c_{k_m}(\hat{i}_c; -T_s)$] ($i > i_c$) becomes smaller than $c_{k_m}(\hat{i}_c; 0)$ or $c_{k_m}(\hat{i}_c; 2T_s)$ [or $c_{k_m}(\hat{i}_c; 0)$ or $c_{k_m}(\hat{i}_c; -2T_s)$]. Using this procedure, the difference (= tracking error) between the peak positions of the true correlation function and its sampled version is minimized as shown in Fig. 4. As described above, the global motion of the arterial wall can be tracked by calculating correlation functions at only 5 lags ($\tau = -2T_s, -T_s, 0, T_s, 2T_s$).

By assigning $k_{m+1} = k_m + \hat{i}_c$ and updating the ROI position as $\hat{x}_1(k_{m+1}) = \hat{x}_1(k_m) + c_0 T_s/2$ (or $\hat{x}_1(k_m) - c_0 T_s/2$), the above procedure is repeated to track the position of the arterial wall throughout one cardiac cycle, as shown in Fig. 5.

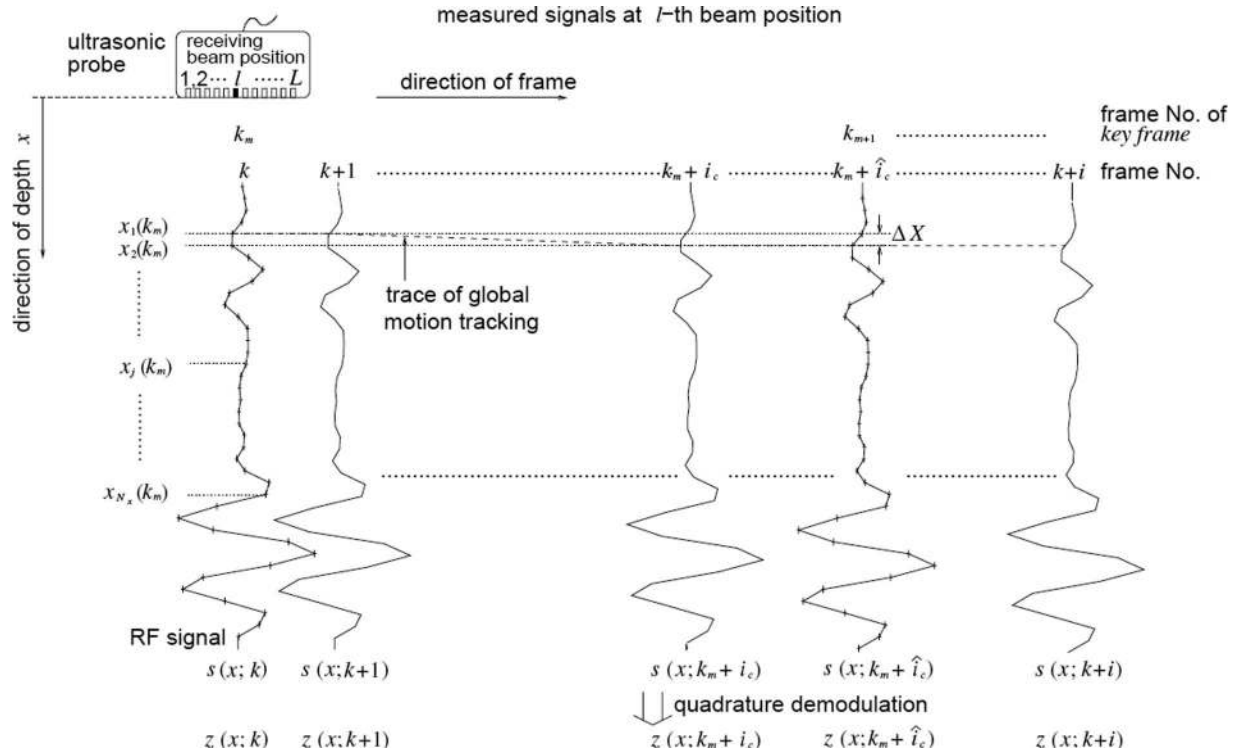


Fig. 5. Illustration of variables.

After the removal of global motion by the above procedure, the residual displacement $u_j(k_m)$ between the k_m th and k_m+1 th frames at each sampled point j ($= 1, 2, \dots, N_X$) along each ultrasonic beam is estimated using the change in the phase of the RF echo [45]–[47]. The residual displacement $u_j(k_m)$ contains global motion because there is small tracking error as shown in Fig. 4. However, it is sufficient to estimate the displacements between the k_m th and k_m+1 th frames because the large global motion is almost removed (tracked) by the above procedure and the residual displacements $\{u_j(k_m)\}$ are subsamples and smaller than half the wavelength of the employed ultrasound. This method of estimation of the displacement distribution significantly reduces the number of calculations (there are many frames between the k_m th and k_m+1 th frames). Radial strain $\varepsilon_{r,j}(k_m)$ is obtained by estimating the spatial gradient of the estimated displacement distribution $\{u_j(k_m)\}$.

III. BASIC EXPERIMENTAL RESULTS

C. Transmitted Sound Field for Parallel Beamforming

Figs 6(a), (b), and (c) show the ultrasonic RF signals measured by a hydrophone (Toray Engineering, Tokyo, H025-002) placed at distances in the depth (axial) direction between the linear array probe and hydrophone of 10 mm, 15 mm, and 20 mm, respectively. The output signal from the hydrophone was acquired with an oscilloscope (Tektronix Japan Ltd., Tokyo, TDS2014) at a sampling frequency of 1 GHz. The hydrophone scanned at every 0.5

mm in the lateral direction using a stage. A plane wave was formed in the depth range from 10 to 20 mm, which corresponds to the typical depth position of the carotid artery. The lateral width of the radiated plane wave is similar to the transmitting aperture width of about 20 mm (96 elements). Fig. 6 shows the waveform of the RF signal and its envelope along the white dashed line in Fig. 6(c). The width at half maximum of the envelope was found to be 0.4 μ s.

B. Comparison of Spatial Resolutions of Conventional Linear Scanning and Parallel Beamforming

Nylon wires (0.1 mm in diameter) embedded in agar (403GS, Gammex, Inc., Middleton, WI) were imaged to investigate the spatial resolution in parallel beamforming.

Figs. 7(a) and (b) show B-mode images obtained by conventional linear scanning and parallel beamforming, respectively. Clear images of the 4 wires were obtained. In the measurement by conventional linear scanning, RF signals focused in real time were acquired at a sampling frequency of 40 MHz.

Fig. 7(c) shows the amplitude profile along the cyan lines in Fig. 7(a) and (b). The widths at half maximum of the amplitude profiles are similar. However, the width at -20 dB is somewhat greater, which worsens the lateral resolution in the B-mode image obtained by parallel beamforming. As shown by these results, parallel beamforming achieves a high frame rate (3472 Hz) at the expense of lateral resolution.

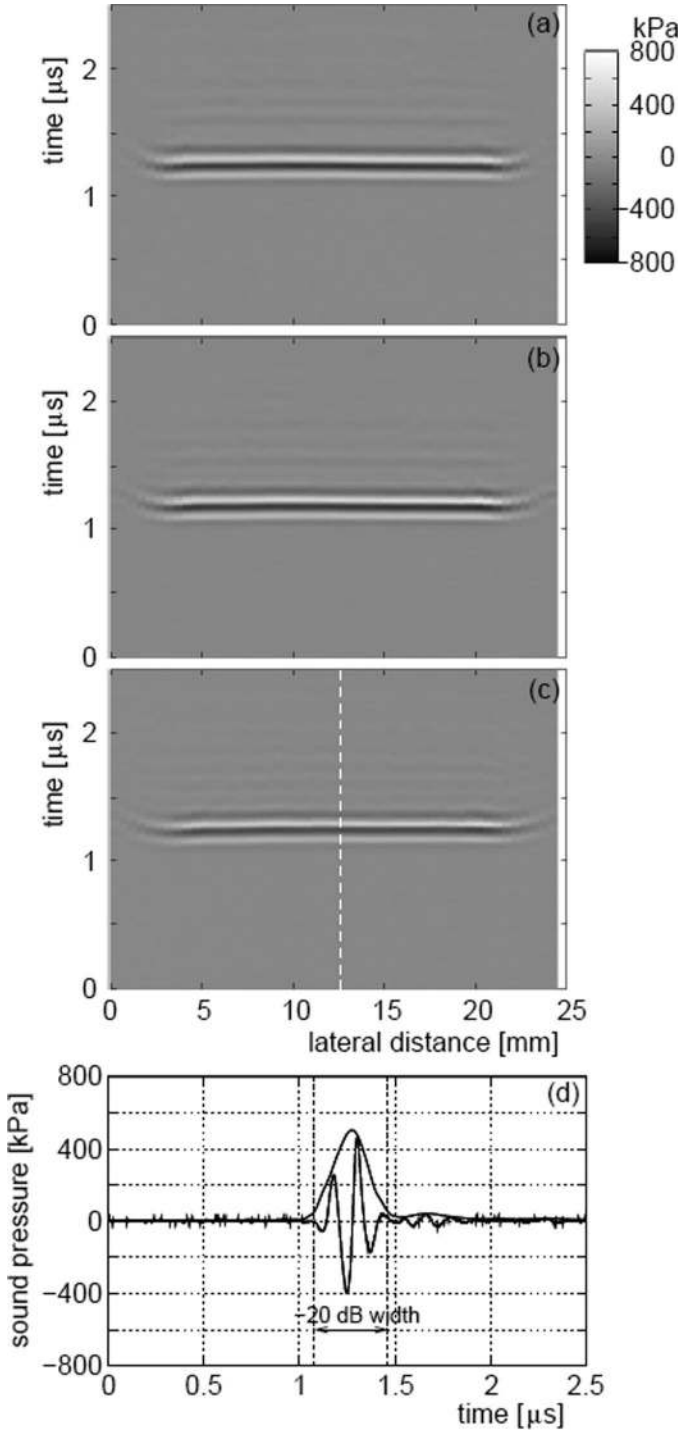


Fig. 6. Ultrasonic RF signals measured by a hydrophone placed at distances between the linear array probe and the hydrophone of (a) 10 mm, (b) 15 mm, and (c) 20 mm. The hydrophone scans in the lateral direction using a stage. (d) Waveform of the RF signal and its envelope along the white dashed line in (c).

The same wires were then imaged with different numbers of elements in receive beamforming. Fig. 8(a) shows a B-mode image of the wires obtained with 88 elements in receive beamforming. Fig. 8(b) shows amplitude profiles along the cyan line in Fig. 8(a) obtained with 4 different numbers of elements in receive beamforming. It is well known that the lateral beam profile depends on the size of

the aperture. As can be seen in Fig. 8(b), a slight degradation of the beam profile was found when 72 elements were employed for receive beamforming. There is a somewhat distinct degradation in the profile obtained with 64 elements, especially in the regions indicated by the dashed ovals in Fig. 8(b). Therefore, the number of elements in receive beamforming was set at 72 in subsequent experiments.

C. Measurements of the Cylindrical Phantom for Evaluation of Accuracy in Strain Estimation

In basic experiments for evaluation of the accuracy of strain estimation, a cylindrical phantom made of silicone rubber was measured by ultrasound. The outer and inner diameters were 10 and 8 mm, respectively. The phantom contained 5% carbon powder (by weight) to obtain sufficient scattering from inside the wall.

Fig. 9 shows a schematic of the measurement system. Change in pressure inside the phantom was induced by circulating a fluid using a flow pump. The change in internal pressure was measured by a pressure sensor (NEC, Tokyo, 9E02-P16). The applied pulse pressure was 48 mmHg.

To measure the elastic moduli of silicone rubber for the calculation of the theoretical strain profile, pressure-diameter testing was conducted. In that testing, the change in external diameter of the phantom was measured with a laser line gauge (KEYENCE, Osaka, VG-035).

1) *Pressure-Diameter Testing*: Fig. 10(a) shows the trigger signal for driving the flow pump. Figs. 10(b) and (c) show waveforms of the internal pressure and change in external diameter of the phantom, respectively. In Fig. 10, the waveforms of 10 measurements are superimposed. From the measured internal pressure, p_i , and the change in external diameter, $2 \cdot \Delta r_o$, the elastic modulus, E , is obtained as follows [49]:

$$E = \frac{3}{2} \frac{r_i^2}{r_o^2 - r_i^2} \frac{p_i}{\varepsilon_\theta} = \frac{3}{2} \frac{r_i^2}{r_o^2 - r_i^2} \frac{p_i}{\frac{\Delta r_o}{r_o}} = \frac{3}{2} \frac{r_i^2 r_o}{r_o^2 - r_i^2} \frac{p_i}{\Delta r_o}, \quad (2)$$

where r_i and r_o are the original internal and external radii, respectively.

In Fig. 10(d), the measured internal pressure is plotted as a function of the change in external diameter Δr_o . The slope, $p_i/\Delta r_o$, was estimated by applying the least-squares method to the measured data shown in Fig. 10(d). The estimated slope, $p_i/\Delta r_o$, is shown by the solid line in Fig. 10(d). Elastic modulus E of the phantom was determined to be 749 kPa.

2) *Estimation of Radial Strain*: Fig. 11(a) shows a longitudinal B-mode image of the phantom obtained by parallel beamforming. In Fig. 11(a), angles ϕ of the receiving beams were 90 degrees. The method for tracking the global motion of the wall (described in Section II-B) was

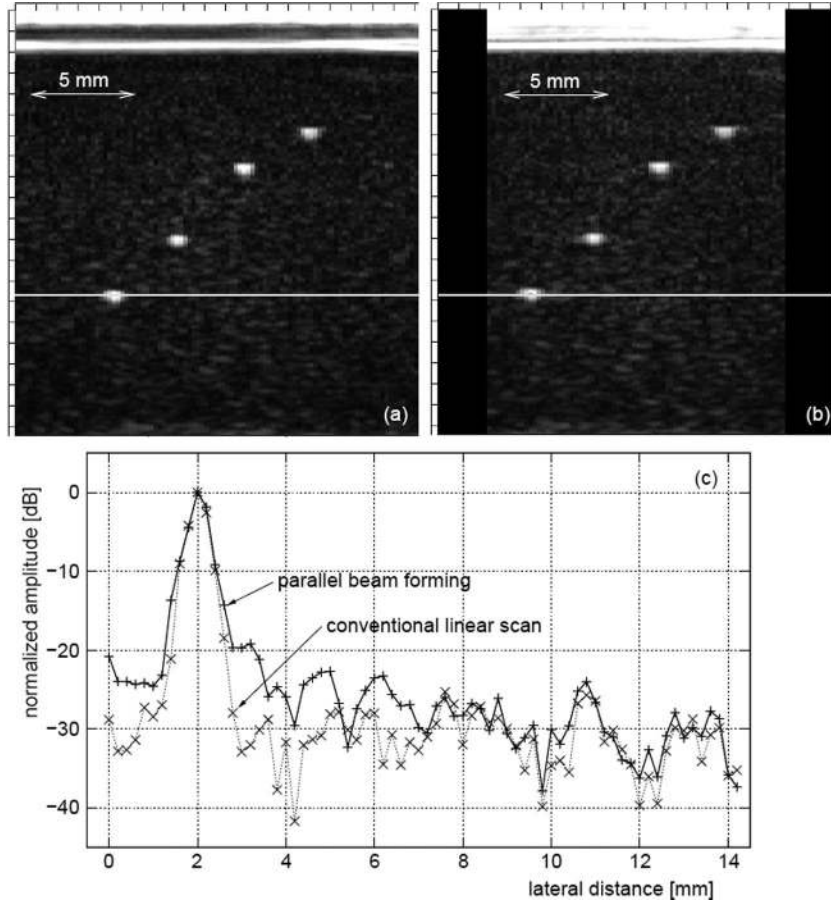


Fig. 7. B-mode images of fine wires embedded in agar: (a) conventional linear scanning; (b) parallel beamforming; and (c) amplitude profiles along the cyan lines in (a) and (b), which are normalized by the maximum amplitudes of the respective profiles.

applied for all 72 ultrasonic beams. The receive beamforming was performed offline based on the method described in Section II-A to create the receiving beams at $\phi = 90$ degrees.

Fig. 11(b) shows RF echoes from the posterior wall along the leftmost beam in Fig. 11(a) during one cycle of the flow pump. In Fig. 11(b), shifts of RF signals in the direction of depth, which are caused by the global motion of the wall, have already been removed. The aligned RF signals show that the global motion of the wall was successfully tracked.

The radial strain distribution in the posterior wall was then estimated by the method described in Section II-B using the phases of RF echoes. In Fig. 11(c), the estimated radial strains are plotted as a function of the distance from the luminal boundary of the posterior wall (in the directions of the ultrasonic beams). Plots and vertical bars show the mean and standard deviation, respectively, at each radial position r , which were obtained by the individual strain distributions along 72 ultrasonic beams. The solid curve in Fig. 11(c) shows the theoretical radial strain $\varepsilon_{r,r}$ of a homogeneous tube at each radial position r , which was obtained using the elastic modulus E measured by pressure-diameter testing and the measured internal pressure as follows [48]:

$$\varepsilon_{r,r} = -\frac{3}{2} \frac{r_i^2 r_o^2}{(r_o^2 - r_i^2) r^2} \frac{p_i}{E}. \quad (3)$$

The estimated strain distribution agrees well with the theoretical strain profile. Mean error e_{mean} and standard deviation SD_{mean} evaluated by (4) and (5) were 4.8% and 9.5%, respectively.

$$e_{\text{mean}} = \frac{1}{N_x} \sum_{j=1}^{N_x} \frac{|E_l[\hat{\varepsilon}_{r,j}] - \varepsilon_{r,r=x_j}|}{|\varepsilon_{r,r=x_j}|}, \quad (4)$$

$$\text{SD}_{\text{mean}} = \frac{1}{N_x} \sum_{j=1}^{N_x} \frac{\sqrt{E_l[(\hat{\varepsilon}_{r,j} - E_l[\hat{\varepsilon}_{r,j}])^2]}}{|\varepsilon_{r,r=x_j}|}, \quad (5)$$

where $E_l[\cdot]$ represents the averaging with respect to beam position l .

IV. IN VIVO SIMULTANEOUS IMAGING OF RADIAL STRAIN AND BLOOD FLOW

The right common carotid artery of a 33-year-old male was measured *in vivo*. Fig. 12(a) shows a B-mode image

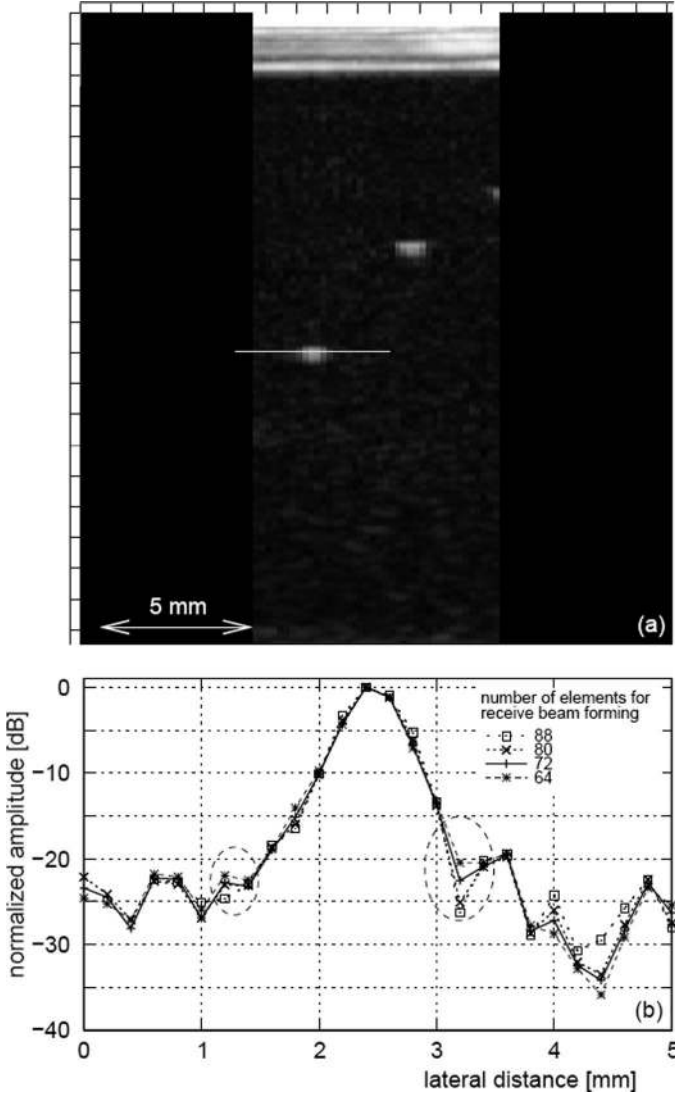


Fig. 8. (a) B-mode image of fine wires embedded in agar obtained with 88 elements in receive beamforming. (b) Amplitude profiles along the cyan line in (a) obtained by four different numbers of elements in receive beamforming.

of the artery obtained by conventional linear scanning. To construct the image in Fig. 12(a), beamformed RF signals sampled at 40 MHz (frame rate: 226 Hz) were envelope-detected, normalized by the maximum amplitude in the image, and then converted into brightness.

Fig. 12(b) shows a B-mode image of the same artery obtained by parallel beamforming. A B-mode image similar to that by conventional linear scanning could be obtained at a very high frame rate of 3472 Hz. To construct the image in Fig. 12(b), RF signals received by the array elements were acquired at a sampling frequency of 40 MHz, and receive beamforming was performed offline based on the method described in Section II-A to form the receiving beams at $\phi = 90$ degrees. As in the creation of the B-mode image in Fig. 12(a), the beamformed RF signals were envelope-detected and converted into brightness. The envelope-detected signals (instantaneous amplitude) were normalized by their maximum value among all frames. Let

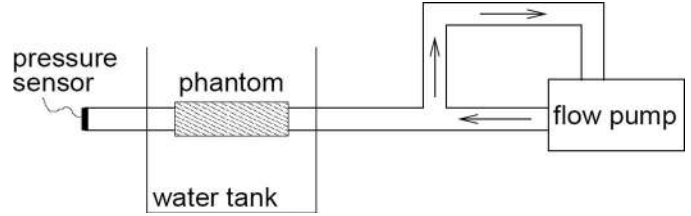


Fig. 9. Schematic of measurement system.

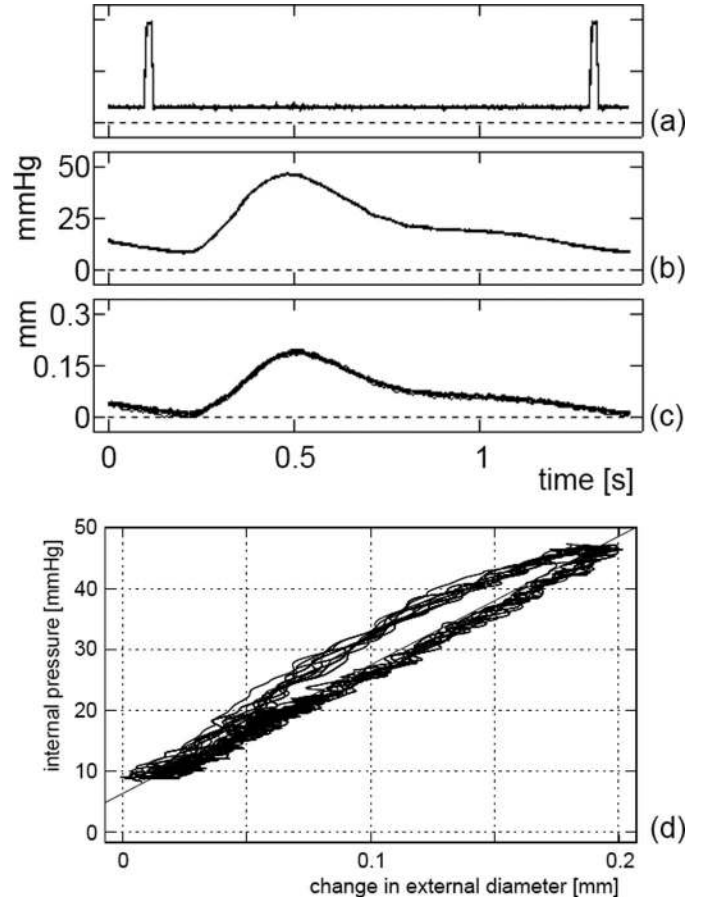


Fig. 10. Waveforms of internal pressure p_i and changes in external diameter Δr_o of the phantom: (a) trigger signal for the flow pump, (b) internal pressure p_i , (c) change in external diameter Δr_o , and (d) relationship between internal pressure p_i and change in external diameter Δr_o .

us define the normalized envelope by $G_p(j; k, k)$, where j , l , and k define depth, beam number, and frame number, respectively. The radial strain of the posterior wall was estimated by applying the same procedure as in Section III-D to the beamformed RF signals.

Blood flow was imaged using ultrasonic beams formed with angles ϕ of 70 and 110 degrees. Obliquely beamformed RF signals were high-pass filtered using the standard double delay line canceler [44]. The powers of the high-pass filtered RF signals were estimated by the conventional power Doppler technique. The number of frames used for calculation of the average power was 64. The roots of the estimated average power were normalized by their

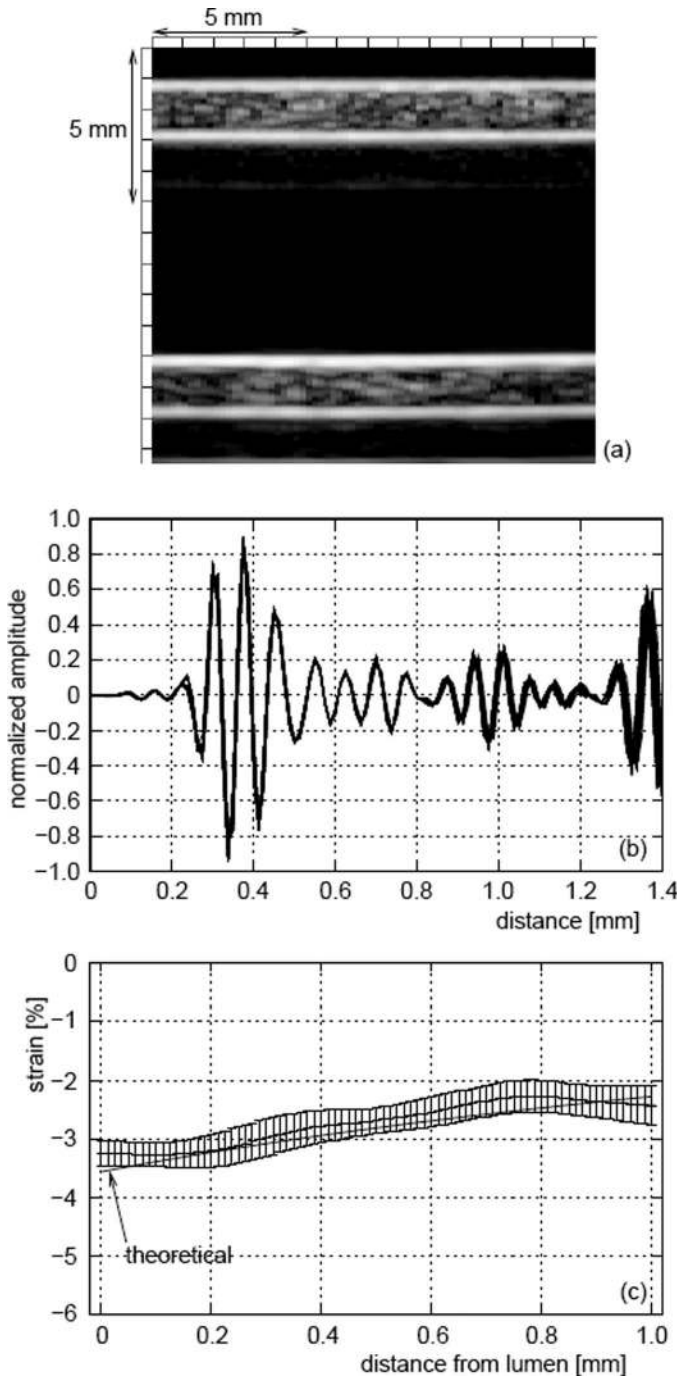


Fig. 11. (a) B-mode image of the phantom in the longitudinal plane and (b) RF signals from the posterior wall during one cycle of the flow pump. Shifts of RF signals in the direction of depth caused by the global motion of the wall have already been compensated for. (c) Radial strains plotted as a function of the distance from the luminal boundary of the posterior wall. Plots and vertical bars are means and standard deviations, respectively, for 72 ultrasonic beams.

maximum among all frames. Let us define the normalized roots of power by $G_{70}(j, l; k)$ and $G_{110}(j, l; k)$ for beam angles ϕ of 70 and 110 degrees, respectively. As shown in Fig. 2, regions scanned by beams at these angles overlap. The normalized root of power, $G_o(j, l; k)$, for obliquely formed beams is defined as in (6) (see next page).

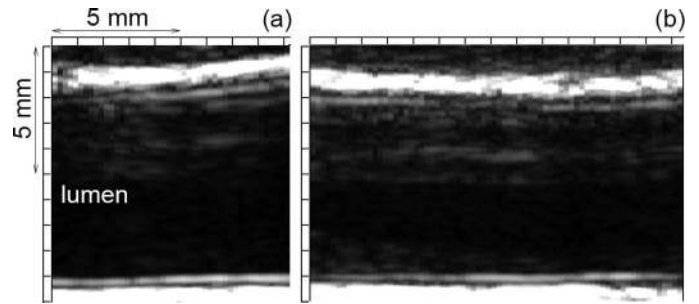


Fig. 12. Longitudinal B-mode image of the right common carotid artery of a 33-year-old male obtained (a) by conventional linear scanning and (b) by ultrasonic beams formed with beam angles ϕ of 90 degrees based on parallel beamforming.

With respect to the shadowed region in the right-hand side of Fig. 2, echo amplitude $G(j, l; k)$ at each point (j, l) in the k th frame is obtained as follows:

$$G(j, l; k) = \alpha G_p(j, l; k) + (1 - \alpha) G_o(j, l; k). \quad (0 \leq \alpha \leq 1) \quad (7)$$

In this study, α was set at 0.9.

Fig. 13(1a) and 13(1b) show images of $G(j, l; k)$ at the R-wave of the electrocardiogram and 0.15 s after the R-wave. As shown in Fig. 13(1b), echoes from blood particles are enhanced when the blood flow velocity is high (at 0.15 s). Fig. 13(1c) shows a blood flow image (at 0.15 s after the R-wave) obtained by receive beamforming with angle ϕ of 90 degrees. By comparing Fig. 13(1b) with Fig. 13(1c), the blood flow imaging was found to be much improved by changing the angle between the directions of blood flow and ultrasonic beam from 90 degrees by oblique receive beamforming ($\phi = 70$ and 110 degrees). Fig. 13(2) shows blood flow images obtained by the same diagnostic equipment based on conventional linear scanning and power Doppler imaging. Although the ability of the conventional method to image the echo signals from blood particles at lower flow rates (in cardiac diastole) is superior to that of the proposed method, the proposed method successfully imaged blood flow.

In Fig. 14, the estimated radial strain at the corresponding time is overlaid on the image of $G(j, l; k)$. The magnitude of the radial strain shown in Fig. 14 was comparable to that of the circumferential strain of about 7%, which was obtained by estimating the global displacements of the anterior and posterior walls at an ultrasonic beam located at the center of the imaged region based on the method described in Section II-B (maximum change in diameter: 480 μm ; original diameter at the R-wave of electrocardiogram: 7 mm). In addition, echoes from the lumen-intima boundary of the posterior wall are visible in the B-mode image shown in Fig. 12(b). In such cases, it has been reported that the strain is stably measured (standard deviation between cardiac cycles: 6.4% [49]). As shown in Fig. 14, the artery-wall strain and blood flow were successfully imaged by the proposed method.

$$G_o(j, l; k) = \begin{cases} G_{70}(j, l; k) \text{ or } G_{110}(j, l; k) & (\text{beams at } \phi = 70 \text{ and } 110 \text{ degrees do not overlap}), \\ \frac{G_{70}(j, l; k) + G_{110}(j, l; k)}{2} & (\text{beams at } \phi = 70 \text{ and } 110 \text{ degrees overlap}). \end{cases} \quad (6)$$

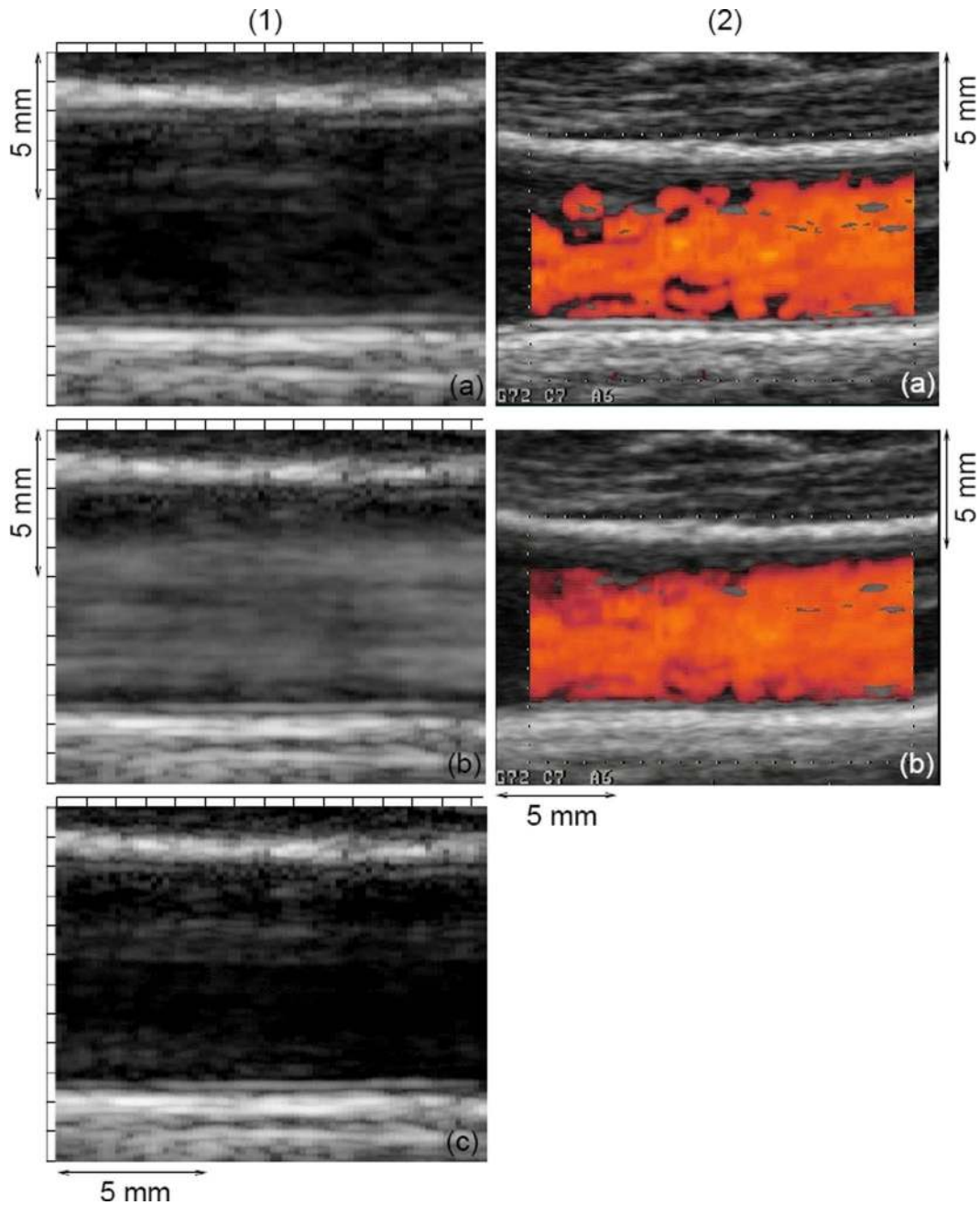


Fig. 13. Blood flow imaging: (1a) and (1b) blood flow images at 0 s and 0.15 s after R-wave of electrocardiogram obtained by parallel beamforming with receive beamforming at $\phi = 70$ and 110 degrees; (1c) blood flow image at 0.15 s after R-wave obtained by parallel beamforming with receive beamforming at $\phi = 90$ degrees; (2a) and (2b) blood flow images obtained by conventional diagnostic equipment based on power Doppler imaging.

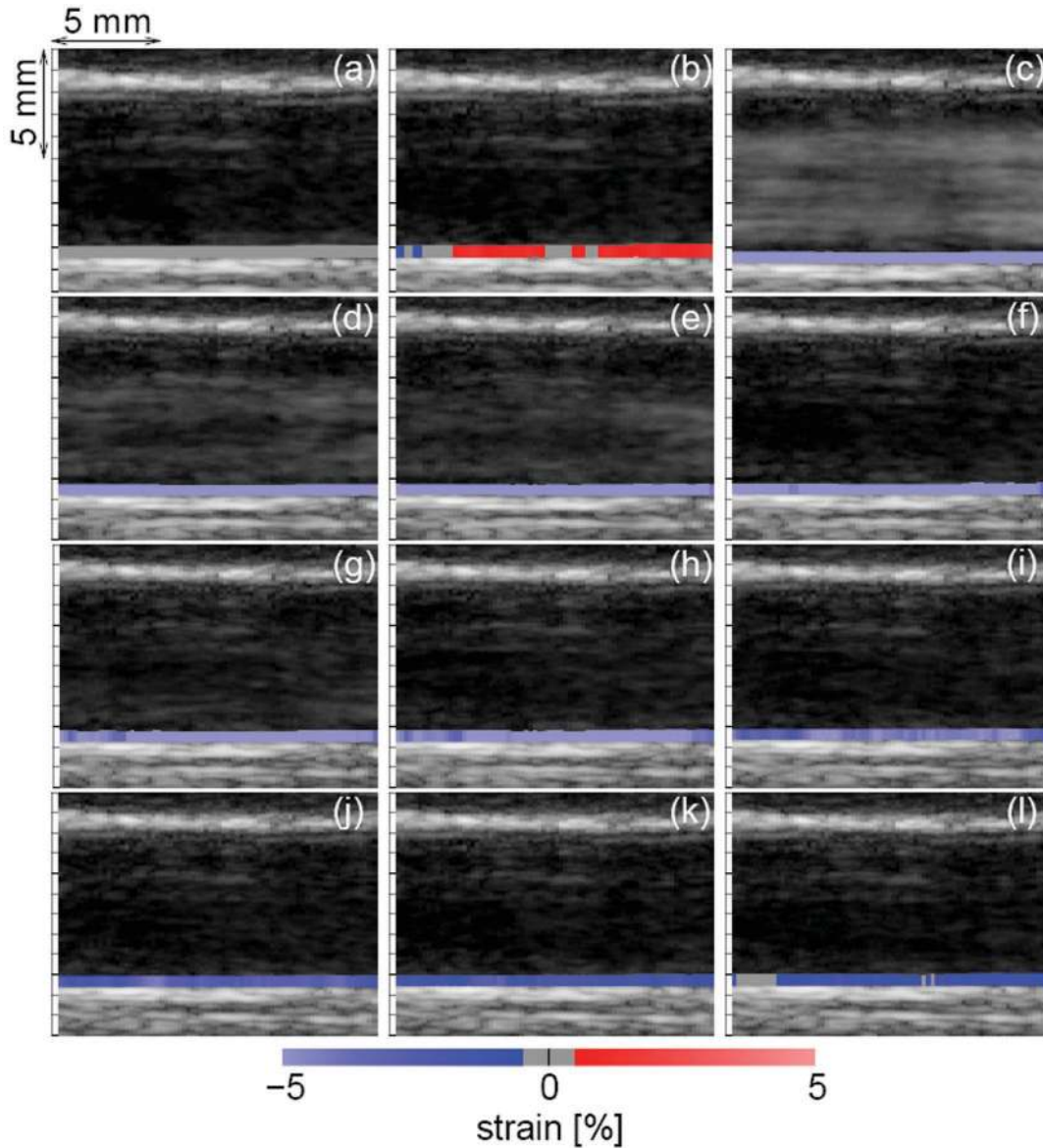



Fig. 14. Simultaneous imaging of artery-wall strain and blood flow. At (a) 0 s, (b) 0.075 s, (c) 0.15 s, (d) 0.225 s, (e) 0.3 s, (f) 0.375 s, (g) 0.45 s, (h) 0.525 s, (i) 0.6 s, (j) 0.75 s, (k) 0.825 s, and (l) 0.9 s after the R-wave of electrocardiogram. 

V. DISCUSSION

In the method herein proposed, the interval of frames between which the phase shift of echoes is estimated (interval of 2 consecutive key frames) is much larger than the original frame rate of 3472 Hz. However, aliasing does not occur because the estimated displacement between 2 key frames is the distance corresponding to the interval of the points sampled, in this study, 19.25 μm (speed of sound: 1540 m/s). Therefore, the residual displacements at other radial positions after compensation of global motion are less than 19.25 μm . When the center frequency of the received RF echo is exactly the same as the nominal center frequency (10 MHz) of the employed ultrasonic probe, a displacement of 19.25 μm produces a phase shift of RF echoes of $\pi/2$ (corresponding to 38.5 μm). The residual

displacement at each radial position after compensation of global motion is smaller than 19.25 μm , which is less than the aliasing limit of 38.5 μm at 10 MHz. In addition, only the strain of the posterior wall was imaged because there were echoes from tissues between the skin surface and the anterior wall, and such echoes would influence the strain estimation. The possible sources of such echoes were the side lobe and multiple reflection. In this study, the influence of the signal-to-noise ratio of the echo signal on the accuracy of strain estimation was not investigated, and a quantitative evaluation of such influences would be required. With respect to the *in vivo* experimental results shown in this paper, the signal-to-noise ratio in the *in vivo* experiment was similar to that in the basic experimental result using the phantom (mean and standard deviation of normalized amplitudes of echoes in all correlation win-

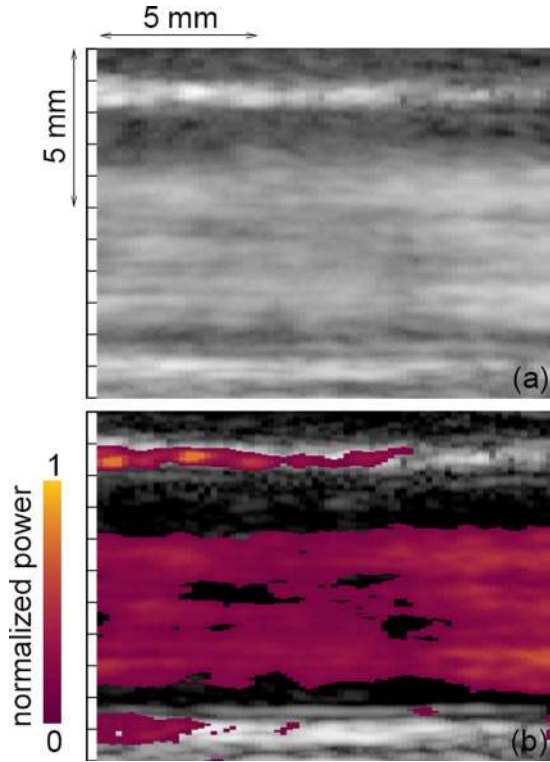


Fig. 15. (a) Blood flow image $G(j, l; k)$ at 0.15 s after R-wave of electrocardiogram obtained by parallel beamforming at $\alpha = 0.5$. (b) Blood flow image at 0.15 s after R-wave obtained by parallel beamforming. Regions where the normalized power $G_o(j, l; k)$ were larger than 0.2 are colored.

dows used for strain estimation: 0.26 ± 0.22 (phantom), 0.19 ± 0.16 (carotid)). Therefore, the accuracy of strain estimation in the *in vivo* experiment was considered to be similar to that in the basic experiment.

In blood flow imaging by parallel beamforming, transmit beams are not focused on and the intensity of radiated ultrasound is much lower than that in conventional linear scanning. Therefore, the high-pass filtered RF signals must be amplified significantly to visualize weak echoes from blood particles. In this process, background noise is also amplified, which leads to degradation of the contrast of the blood flow image $G(j, l; k)$ (Fig. 13(1-a)) in comparison with the B-mode image $G_p(j, l; k)$, shown in Fig. 12(b). Image degradation at lower α in (7) is significant due to the amplification of noise as shown in Fig. 15(a); the image in Fig. 15(a) was obtained at $\alpha = 0.5$. To avoid a significant degradation of a blood flow image, α was empirically assigned by an operator.

The parameter α was introduced because the discrimination of echoes from blood particles from those from slowly moving tissue by high-pass filtration was not sufficient. To improve the discrimination, receiving beams were obliquely formed (steered angle: ± 20 degrees). However, the discrimination was not still sufficient. Colored regions in Fig. 15(b) show the regions where the normalized root of power $G_o(j, l; k)$ for obliquely formed beams is larger than 0.2. As shown in Fig. 15(b), clutter from the arterial wall was not perfectly removed. Therefore, in

this study, blood flow was displayed in gray scale based on (7) without thresholding. Further investigation is required for improving the discrimination (e.g., increase in the intensity of a transmit beam and improvement of clutter filtering).

As described above, in this study, blood flow was qualitatively imaged by high-pass filtering of received RF echoes. Ultrasonic beams for blood flow imaging were formed at 2 different beam angles, the angles of these ultrasonic beams relative to the direction of blood flow being different. Therefore, there would be discontinuities in an image when the flow velocity is quantitatively imaged based on the standard Doppler technique because the estimation of flow velocity significantly depends on the angle between the direction of flow and the ultrasonic beam. In future work, the quantitative estimation of blood flow velocity will be investigated to overcome such problems.

In this study, RF signals received by transducer elements were acquired for offline receive beamforming. In the current system, processing of dynamic focusing at 3 different beam angles and calculation of strain and blood flow is difficult during a frame interval of about 0.3 ms (at a frame rate of 3500 Hz). Real-time implementation of the proposed method requires further optimization of the algorithm and development of specific hardware. In addition, an automated method for detection of the arterial wall in ultrasound data needs to be developed for real-time processing.

VI. CONCLUSIONS

In this study, a high frame rate acquisition of RF echoes (3472 Hz) was achieved using parallel beamforming, which realizes the simultaneous imaging of the artery-wall strain and blood flow. In the estimation of strain, the global motion of the arterial wall was tracked based on the correlation between RF signals, and the displacement distribution in the wall was then estimated using the phases of RF signals. The accuracy of the strain estimation was validated by a basic experiment using a cylindrical phantom. Furthermore, the wall strain and blood flow of a carotid artery was successfully imaged *in vivo*. The proposed method would provide useful information for diagnosis of atherosclerosis.

APPENDIX

RELATIONSHIP BETWEEN STEERING BEAM ANGLE AND GRATING LOBE

The directivity of a linear array $D(\psi)$ can be expressed as the product of the directivity of an array $D_a(\psi)$ and that of an element $D_e(\psi)$ [43] as follows:

$$D(\psi) = D_e(\psi) \cdot D_a(\psi), \quad (8)$$

where the angle ψ is defined as $\psi = 90^\circ - \phi$. The directivity $D_a(\psi)$ shows that of an array composed of omnidirectional point sources (elements), and $D_a(\psi)$ is expressed by the number of sources N_e and the spacing of sources d as follows:

$$D_a(\psi) = \frac{\sin \left\{ \frac{N_e \pi d}{\lambda} (\sin \psi - \sin \psi_0) \right\}}{N_e \sin \left\{ \frac{\pi d}{\lambda} (\sin \psi - \sin \psi_0) \right\}}, \quad (9)$$

where ψ_0 and λ are the steering angle and wavelength of ultrasound in tissue, respectively. The directivity of an rectangular element $D_e(\psi)$ is expressed by the width of an element w as follows:

$$D_e(\psi) = \frac{\sin \left(\frac{\pi w}{\lambda} \sin \psi \right)}{\frac{\pi w}{\lambda} \sin \psi}. \quad (10)$$

ACKNOWLEDGMENTS

We are grateful to Panasonic Co., Ltd. for providing the cylindrical phantom used in this study.

REFERENCES

- [1] R. T. Lee, A. J. Grodzinsky, E. H. Frank, R. D. Kamm, and F. J. Schoen, "Structure-dependent dynamic mechanical behavior of fibrous caps from human atherosclerotic plaques," *Circulation*, vol. 83, no. 5, pp. 1764–1770, 1991.
- [2] H. M. Loree, A. J. Grodzinsky, S. Y. Park, L. J. Gibson, and R. T. Lee, "Static circumferential tangential modulus of human atherosclerotic tissue," *J. Biomech.*, vol. 27, no. 2, pp. 195–204, 1994.
- [3] M. Benthin, P. Dahl, R. Ruzicka, and K. Lindström, "Calculation of pulse-wave velocity using cross-correlation—effects of reflexes in the arterial tree," *Ultrasound Med. Biol.*, vol. 17, no. 5, pp. 461–469, 1991.
- [4] H. Kanai, K. Kawabe, M. Takano, R. Murata, N. Chubachi, and Y. Koiwa, "New method for evaluating local pulse wave velocity by measuring vibrations on aortic wall," *Electron. Lett.*, vol. 30, no. 7, pp. 534–536, 1993.
- [5] P. J. Brands, J. M. Willigers, L. A. F. Ledoux, R. S. Reneman, and A. P. G. Hoeks, "A noninvasive method to estimate pulse wave velocity in arteries locally by means of ultrasound," *Ultrasound Med. Biol.*, vol. 24, no. 9, pp. 1325–1335, 1998.
- [6] A. Eriksson, E. Greiff, T. Loupas, M. Persson, and P. Pesque, "Arterial pulse wave velocity with tissue Doppler imaging," *Ultrasound Med. Biol.*, vol. 28, no. 5, pp. 571–580, 2002.
- [7] J. M. Meinders, P. J. Brands, J. M. Willigers, L. Kornet, and A. P. G. Hoeks, "Assessment of the spatial homogeneity of artery dimension parameters with high frame rate 2-D B-mode," *Ultrasound Med. Biol.*, vol. 27, no. 6, pp. 785–794, 2001.
- [8] A. P. G. Hoeks, C. J. Ruijsen, P. Hick, and R. S. Reneman, "Transcutaneous detection of relative changes in artery diameter," *Ultrasound Med. Biol.*, vol. 11, no. 1, pp. 51–59, 1985.
- [9] T. Länne, H. Stale, H. Bengtsson, D. Gustafsson, D. Bergqvist, B. Sonesson, H. Lecerof, and P. Dahl, "Noninvasive measurement of diameter changes in the distal abdominal aorta in man," *Ultrasound Med. Biol.*, vol. 18, no. 5, pp. 451–457, 1992.
- [10] P. J. Brands, A. P. G. Hoeks, M. C. M. Rutten, and R. S. Reneman, "A noninvasive method to estimate arterial impedance by means of assessment of local diameter change and the local center-line blood flow velocity using ultrasound," *Ultrasound Med. Biol.*, vol. 22, no. 7, pp. 895–905, 1996.
- [11] J. Ophir, I. Céspedes, H. Ponnekanti, Y. Yazdi, and X. Li, "Elastography: A quantitative method for imaging the elasticity of biological tissues," *Ultrason. Imaging*, vol. 13, no. 2, pp. 111–134, Apr. 1991.
- [12] I. Céspedes and J. Ophir, "Reduction of image noise in elastography," *Ultrason. Imaging*, vol. 15, no. 2, pp. 89–102, Apr. 1993.
- [13] E. E. Konofagou, J. Ophir, T. Varghese, and F. Kallel, "A new elastographic method for estimation and imaging of lateral displacements, lateral strains, corrected axial strain and Poisson's ratios in tissues," *Ultrasound Med. Biol.*, vol. 24, no. 8, pp. 1183–1199, 1998.
- [14] J. Ophir, B. Garra, F. Kallel, E. Konofagou, T. Krouskop, R. Righetti, and T. Varghese, "Elastographic imaging," *Ultrasound Med. Biol.*, vol. 26, pp. S23–S29, May 2000.
- [15] C. L. de Korte, E. I. Céspedes, A. F. W. van der Steen, and C. T. Lancée, "Intravascular elasticity imaging using ultrasound: Feasibility studies in phantoms," *Ultrasound Med. Biol.*, vol. 23, no. 5, pp. 735–746, 1997.
- [16] E. I. Céspedes, C. L. de Korte, and A. F. W. van der Steen, "Intraluminal ultrasonic palpation: Assessment of local and cross-sectional tissue stiffness," *Ultrasound Med. Biol.*, vol. 26, no. 3, pp. 385–396, 2000.
- [17] O. Bonnefous, "Blood flow and tissue motion with ultrasound for vascular applications," *Comptes Rendus de l'Académie des Sciences—Series IV—Physics*, vol. 2, pp. 1161–1178, 2001.
- [18] R. L. Maurice, J. Ohayon, Y. Frétygn, M. Bertrand, G. Soulez, and G. Cloutier, "Noninvasive vascular elastography: Theoretical framework," *IEEE Trans. Med. Imaging*, vol. 23, no. 2, pp. 164–180, 2004.
- [19] H. Ribbers, S. Holewijn, J. D. Blankensteijn, and C. L. de Korte, "Non-invasive two dimensional elastography of the carotid artery," in *Proc. 2005 IEEE Ultrasonics Symp.*, pp. 1113–1116.
- [20] K. Kim, W. F. Weitzel, J. M. Rubin, H. Xie, X. Chen, and M. O'Donnell, "Vascular intramural strain imaging using arterial pressure equalization," *Ultrasound Med. Biol.*, vol. 30, no. 6, pp. 761–771, 2004.
- [21] M. A. Lubinski, S. Y. Emelianov, and M. O'Donnell, "Speckle tracking methods for ultrasonic elasticity imaging using short-time correlation," *IEEE Trans. Ultrason. Ferroelectr. Freq. Control*, vol. 46, no. 1, pp. 82–96, 1999.
- [22] E. Brusseau, J. Fromageau, G. Finet, P. Delachartre, and D. Vray, "Axial strain imaging of intravascular data: Results on polyvinyl alcohol cryogel phantoms and carotid artery," *Ultrasound Med. Biol.*, vol. 27, no. 12, pp. 1631–1642, 2001.
- [23] H. Kanai, M. Sato, Y. Koiwa, and N. Chubachi, "Transcutaneous measurement and spectrum analysis of heart wall vibrations," *IEEE Trans. Ultrason. Ferroelectr. Freq. Control*, vol. 43, no. 5, pp. 791–810, 1996.
- [24] H. Hasegawa, H. Kanai, Y. Koiwa, and N. Chubachi, "Noninvasive evaluation of Poisson's ratio of arterial wall using ultrasound," *Electron. Lett.*, vol. 33, no. 4, pp. 340–342, 1997.
- [25] H. Kanai, H. Hasegawa, N. Chubachi, Y. Koiwa, and M. Tanaka, "Noninvasive evaluation of local myocardial thickening and its color-coded imaging," *IEEE Trans. Ultrason. Ferroelectr. Freq. Control*, vol. 44, no. 4, pp. 752–768, 1997.
- [26] H. Kanai, Y. Koiwa, and J. Zhang, "Real-time measurements of local myocardium motion and arterial wall thickening," *IEEE Trans. Ultrason. Ferroelectr. Freq. Control*, vol. 46, no. 5, pp. 1229–1241, 1999.
- [27] H. Hasegawa, H. Kanai, and Y. Koiwa, "Modified phased tracking method for measurement of change in thickness of arterial wall," *Jpn. J. Appl. Phys.*, vol. 41, no. 5B, pp. 3563–3571, 2002.
- [28] H. Hasegawa, H. Kanai, N. Hoshimiya, and Y. Koiwa, "Evaluating the regional elastic modulus of a cylindrical shell with non-uniform wall thickness," *J. Med. Ultrason.*, vol. 31, no. 2, pp. 81–90, 2004.
- [29] H. Kanai, H. Hasegawa, M. Ichiki, F. Tezuka, and Y. Koiwa, "Elasticity imaging of atheroma with transcutaneous ultrasound—Preliminary study," *Circulation*, vol. 107, no. 24, pp. 3018–3021, 2003.
- [30] J. Inagaki, H. Hasegawa, H. Kanai, M. Ichiki, F. Tezuka, and Y. Koiwa, "Construction of reference data for tissue characterization of arterial wall based on elasticity images," *Jpn. J. Appl. Phys.*, vol. 44, no. 6B, pp. 4593–4597, 2005.

- [31] J. Inagaki, H. Hasegawa, H. Kanai, M. Ichiki, F. Tezuka, and Y. Koiwa, "Tissue classification of arterial wall based on elasticity image," *Jpn. J. Appl. Phys.*, vol. 45, no. 5B, pp. 4732–4735, 2006.
- [32] M. I. Plett, K. W. Beach, B. Dunmire, K. G. Brown, J. F. Primozich, and E. Strandness Jr., "In vivo ultrasonic measurement of tissue vibration at a stenosis: A case study," *Ultrasound Med. Biol.*, vol. 27, no. 8, pp. 1049–1058, 2001.
- [33] P. Tortoli, T. Morganti, G. Bambi, C. Palombo, and K. V. Ramnarine, "Noninvasive simultaneous assessment of wall shear rate and wall distension in carotid arteries," *Ultrasound Med. Biol.*, vol. 32, no. 11, pp. 1661–1670, 2006.
- [34] M. C. Corretti, T. J. Anderson, E. J. Benfamin, D. Celermajer, F. Charbonneau, M. A. Creager, J. Deanfield, H. Drexler, M. Gehard-Herman, D. Herrington, P. Vallance, J. Vita, and R. Vogel, "Guidelines for the ultrasound assessment of endothelial-dependent flow-mediated vasodilation of the brachial artery," *J. Am. Coll. Cardiol.*, vol. 39, no. 2, pp. 257–265, 2002.
- [35] T. Kaneko, H. Hasegawa, and H. Kanai, "Ultrasonic measurement of change in elasticity due to endothelium dependent relaxation response by accurate detection of artery-wall boundary," *Jpn. J. Appl. Phys.*, vol. 46, no. 7B, pp. 4881–4888, 2007.
- [36] K. Ikeshita, H. Hasegawa, and H. Kanai, "Ultrasonic measurement of transient change in the stress-strain property of radial arterial wall caused by endothelial-dependent vasodilation," *Jpn. J. Appl. Phys.*, vol. 47, no. 5, pp. 4165–4169, 2008.
- [37] S. I. Nikolov and J. A. Jensen, "In-vivo synthetic aperture flow imaging in medical ultrasound," *IEEE Trans. Ultrason. Ferroelectr. Freq. Control*, vol. 50, no. 7, pp. 848–856, 2003.
- [38] Y. Minochi, S. Yagi, and T. Nishiyama, "Estimation of local displacement vector in random medium utilizing synthetic aperture array signal processing," *Jpn. J. Appl. Phys.*, vol. 43, no. 5B, pp. 3103–3106, 2004.
- [39] M. Tanter, J. Bercoff, L. Sandrin, and M. Fink, "Ultrafast compound imaging for 2-D motion vector estimation: Application to transient elastography," *IEEE Trans. Ultrason. Ferroelectr. Freq. Control*, vol. 49, no. 10, pp. 1363–1374, 2002.
- [40] G. R. Lockwood, J. R. Talman, and S. S. Brunke, "Real-time 3-D ultrasound imaging using sparse synthetic aperture beamforming," *IEEE Trans. Ultrason. Ferroelectr. Freq. Control*, vol. 45, no. 4, pp. 980–988, 1998.
- [41] S. Ishigami, H. Yanagida, Y. Tamura, C. Ishihara, and N. Okada, "Observation of dynamic structure using ultrasound 3D imaging system with encoded wave front," *Jpn. J. Appl. Phys.*, vol. 42, no. 5B, pp. 3276–3280, 2003.
- [42] O. T. von Ramm, S. W. Smith, and H. G. Pavy Jr., "High-speed ultrasound volumetric imaging system. II. Parallel processing and image display," *IEEE Trans. Ultrason. Ferroelectr. Freq. Control*, vol. 38, no. 2, pp. 109–115, 1991.
- [43] F. J. Pompei and S. Wooh, "Phased array element shapes for suppressing grating lobes," *J. Acoust. Soc. Am.*, vol. 111, no. 5, pp. 2040–2048, 2002.
- [44] B. R. Mahafza, *Introduction to Radar Analysis*. Boca Raton, FL: CRC Press, 1998.
- [45] H. Hasegawa and H. Kanai, "Strain imaging of arterial wall with translational motion compensation and error correction," in *Proc. 2007 IEEE Ultrasonics Symp.*, pp. 860–863.
- [46] H. Hasegawa and H. Kanai, "Reduction of influence of variation in center frequencies of RF echoes on estimation of artery-wall strain," *IEEE Trans. Ultrason. Ferroelectr. Freq. Control*, vol. 55, no. 9, pp. 1921–1934, 2008.
- [47] H. Hasegawa and H. Kanai, "Modification of the phased-tracking method for reduction of artifacts in estimated artery wall deformation," *IEEE Trans. Ultrason. Ferroelectr. Freq. Control*, vol. 53, no. 11, pp. 2050–2064, 2006.
- [48] S. P. Timoshenko and J. N. Goodier, *Theory of Elasticity*, 3rd ed. New York: McGraw Hill, 1970.
- [49] N. Nakagawa, H. Hasegawa, and H. Kanai, "Cross-sectional elasticity imaging of carotid arterial wall in short-axis plane by transcutaneous ultrasound," *Jpn. J. Appl. Phys.*, vol. 43, no. 5B, pp. 3220–3226, 2004.



Hideyuki Hasegawa was born in Oyama, Japan, in 1973. He received the B.E. degree from Tohoku University, Sendai, Japan, in 1996. He received the Ph.D. degree from Tohoku University in 2001. He is presently an associate professor at the Graduate School of Biomedical Engineering, Tohoku University. His main research interest is medical ultrasound, especially diagnosis of atherosclerosis based on measurements of motion and mechanical properties of the arterial wall. Dr. Hasegawa is a member of the IEEE, the Acoustical Society of Japan, the Japan Society of Ultrasonics in Medicine, and the Institute of Electronics, Information and Communication Engineers.



Hiroshi Kanai was born in Matsumoto, Japan, on November 29, 1958. He received a B.E. degree from Tohoku University, Sendai, Japan, in 1981, and M.E. and Ph.D. degrees in electrical engineering, also from Tohoku University, in 1983 and 1986, respectively. From 1986 to 1988, he was with the Education Center for Information Processing, Tohoku University, as a research associate. From 1990 to 1992, he was a lecturer in the Department of Electrical Engineering, Faculty of Engineering, Tohoku University. From 1992 to 2001, he was an associate professor in the Department of Electrical Engineering, Faculty of Engineering, Tohoku University. Since 2001, he has been a professor in the Department of Electronic Engineering, Graduate School of Engineering, Tohoku University.

His present interests are in ultrasonic measurement and digital signal processing for diagnosis of heart diseases and arteriosclerosis. Dr. Kanai is a member of the Acoustical Society of Japan, the Institute of Electronics Information and Communication Engineering of Japan, the Japan Society of Ultrasonics in Medicine, Japan Society of Medical Electronics and Biological Engineering, and the Japanese Circulation Society.